Bioactive Materials 28 (2023) 432–447

Contents lists available at ScienceDirect

Bioactive Materials

journal homepage: www.keaipublishing.com/en/journals/bioactive-materials

Enhanced osseointegration of drug eluting nanotubular dental implants: An *in vitro* and *in vivo* study

Pankaj Chauhan [a,b], Alok Srivastava [c], Pooja Bhati [c,d], Manish Chaturvedi [c,e], Vinay Patil [c], Sriram Kunnoth [f], Nisha Kumari [c], Vedpal Arya [c,g], Madhur Pandya [c], Mohit Agarwal [c], Smiti Bhardwaj [h], Farrukh Faraz [h], Sanjay Chauhan [i], Mahesh Verma [j], Veena Koul [b], Naresh Bhatnagar [c,*]

[a] *Homi Bhabha Cancer Hospital and Research Centre, Vizag, Andhra Pradesh, India*
[b] *Centre for Biomedical Engineering, Indian Institute of Technology Delhi, India*
[c] *Department of Mechanical Engineering, Indian Institute of Technology Delhi, India*
[d] *Mechanical & Automation Engineering, Indira Gandhi Delhi Technical University for Women, New Delhi, India*
[e] *Rajasthan Technical University, Kota Rajasthan, India*
[f] *Applied Mechanics, Indian Institute of Technology Delhi, India*
[g] *National University of Singapore, Singapore*
[h] *Department of Periodontics, Maulana Azad Institute of Dental Sciences, New Delhi, India*
[i] *Rajasthan Dental College and Hospital, Jaipur, Rajasthan, India*
[j] *Department of Prosthodontics, Maulana Azad Institute of Dental Sciences, New Delhi, India*

ARTICLE INFO

Keywords:
Titanium
Biocompatibility
Simvastatin
Nanotube
Micro CT
Histopathology
Nanoscale

ABSTRACT

Faster and predictable osseointegration is crucial for the success of dental implants, especially in patients with compromised local or systemic conditions. Despite various surface modifications on the commercially available Titanium (Ti) dental implants, the bioactivity of Ti is still low. Thus, to achieve both biological and therapeutic activity on titanium surfaces, surface modification techniques such as titanium nanotubes have been studied as nanotube surfaces can hold therapeutic drugs and molecules. The main aim of the present research work is to study the early osseointegration around the novel Simvastatin drug eluting nanotubular dental implant. In the present research, the titanium nanotubes were fabricated on the screw-shaped dental implant surface and the Simvastatin drug was loaded into the nanotubes using the ultrasonication dip method. *In vitro and In vivo* studies were carried out on the modified dental implants. *In vitro* cell culture study reported enhanced osteogenic activity on the drug-loaded nanotube surface implants. The *in vivo* animal studies were evaluated by micro-CT, histopathology, and reverse torque removal analysis methods. The test results showed faster osseointegration with the strong interface on the Simvastatin drug-loaded implant surface at 4 weeks of healing as compared to the control implants.

1. Introduction

Titanium and its alloys are the preferred gold standard biomaterial for dental implant fabrication. Owing to their superior biocompatibility, mechanical properties, and corrosion resistance, favorable long-term osseointegration is predictable around Ti dental implants [1]. Osseointegration plays a vital role in the success of dental implants. It is defined as a direct apposition of living bone at the bone-implant interface and is considered a prerequisite for the long-term clinical success of dental implants [1]. However. it is influenced by several factors including the implant's material, surface topography, geometrical features, and clinical factors. The reported survival rate of titanium dental implants is very high compared to other implanted devices [2,3]. Despite the favorable survival rates, the osseointegration process of titanium dental implants requires a longer healing period due to its bioinert properties [4]. Apart from this, the incidence of implant failure is high in

Peer review under responsibility of KeAi Communications Co., Ltd.
* Corresponding author.
E-mail address: nareshb@mech.iitd.ac.in (N. Bhatnagar).

https://doi.org/10.1016/j.bioactmat.2023.06.003
Received 28 December 2022; Received in revised form 16 May 2023; Accepted 5 June 2023

compromised clinical situations such as decreased bone quality/quantity and systemic conditions like osteoporosis. Hence, there is a need to augment the bioactivity of titanium surfaces.

In the past various surface modifications have been performed at the macro and micro-scales, aiming to enhance the bioactivity and accelerate the osseointegration process. Briefly, these include roughening by blasting with hydroxyapatite/alumina, acid etching, coating by TiO_2/hydroxyapatite, polymer coating, and various other topography modifications [5]. Also, diverse surface coatings with different biomaterials and biomolecules have been explored in recent decades to gain therapeutic activity and faster osseointegration. For example, the coating of calcium phosphates and hydroxyapatite (HA) like biomaterials enhance surface bioactivity and improve osseointegration [5]. Similarly, the coating of implants with various pharmacological agents like bisphosphonates, antibiotics, antimicrobial peptides, and biomolecules has been reported with promising outcomes in terms of surface properties and therapeutic effects [6]. However, to achieve beneficial therapeutic effects like reduced bacterial activity, and enhanced osteoblastic activity, the controlled and prolonged release of therapeutic agents is desired. Thus, the surface coating should sustain the shear forces during the implant insertion inside the bone. The major limitations of the coating methods are descaling, delamination, or debonding during the implant insertions and therapeutic agents cannot be delivered at a sustained rate [6].

Investigations over the last two decades have established that nanoscale topography can augments and even outperform cellular functions compared to macro and microtopography [7]. Additionally, these studies have also revealed that nano surfaces possess immunomodulatory and antibacterial effects which could influence the short and long-term osseointegration of dental implants [8,9].

Electrochemical anodization of titanium surface stands out as a recent method to modify the titanium dental implant surface at the nano level due to their ability to form nanotubes on the complex geometry of dental implant surface. These modified nanotube surfaces possess enhanced bioactivity and can hold drugs for local elution [10]. Moreover, this method has a great degree of control over the dimensions of nanoscale features and is a cost-effective method. In the recent past research has been done in this area regarding the fabrication of highly ordered TiO_2 nanostructures and the optimization of their bioactivity and drug-eluting properties [11].

For the clinical translation of the newly developed implant surface, rigorous step-by-step testing is required to evaluate the biocompatibility and osseointegration capability. In the works of literature, various *in vitro* and *in vivo* methods have been used for the evaluation of osseointegration [12]. *In vitro* testing includes cell adhesion, proliferation, differentiation assays, and osteogenic gene marker studies [13]. These tests provide information regarding cytotoxicity, and cytocompatibility thus, providing baseline understanding and reducing the number of animals required for *in vivo* testing. However, *in vitro* studies cannot demonstrate the tissue response to materials, as the response is confined to individual cells. Moreover, the design of the implant (e.g., conical shape, screw) also has a considerable impact on the primary bone anchorage, hence on osseointegration. So, a detailed in-vivo sequential study is needed on the newly developed surfaces. Histomorphometry and reverse torque removal are the most commonly used method for the evaluation of osseointegration around dental implants in animal models [14,15]. Presently, micro-CT is also used widely due to its added advantage in the evaluation of osseointegration as it can provide multiple-section information and the same sample can be reused for further testing [16,17].

The role of surface microtopography is well established in the literature and recent studies have also shown that graded nano microtopography performs better than only micro or nanotopography [18]. As per *Wang et al.* nanotubes in the range of 70–100 nm possess more bone cell attachment, proliferation, and differentiation activity *in vitro* and more bone apposition *in vivo* [19]. Furthermore, various drugs have been used to accelerate the process of osseointegration [20]. Although Simvastatin is a cholesterol-lowering drug, it has an enhancing role in the osseointegration process [21–23]. It is hypothesized that it can promote bone growth via stimulation of BMP-2 expression [21,22].

In the present research, the nanotubes (diameter of ≈80 nm) were fabricated over the micro rough surface of screw-shaped dental implants, so that a nano-micro graded surface can be achieved. Further, these nanotubes were loaded with the optimized concentration of the Simvastatin drug. Several clinical trials have demonstrated that Sand-blasted large grit and acid-etched (SLA) implant surfaces integrate better into bone than conventional smooth, blasted, or only acid-etched surfaces [24–26]. A classic SLA surface was also prepared on titanium implants in the present research work and it was also used as the control implants along with machined implants [24–26].

The main aim of the present research is to evaluate the osseointegration capabilities of the nanotubular and Simvastatin-loaded nanotubular implants in comparison to machined and SLA surface dental implants. The major research objective includes: 1. Fabrication of the titanium nanotubes on the complex geometry and rough surface of the dental implant and loading of optimized concentration of Simvastatin drugs inside the nanotubes. *2.* Comparison and evaluation of the cytocompatibility of nanotubes and Simvastatin-loaded nanotubes surfaces. *3.* Assessment of the early osseointegration around nanotubular and drug-loaded nanotubular dental implants in an animal model.

2. Materials and methods

2.1. Samples preparation

The disc samples (n = 120, diameter- 5 mm) and screw-shaped dental implants (n = 72, diameter 3.5 mm and length 8 mm) was machined on a 10-axis CNC turn-mill from Ti6Al4V alloy ELI grade material. Screw-shaped dental implants designs were opted from the previous work *Chauhan et al.* [27, 28]. However, for animal study, slight modifications were made where an apical bone growth chamber of diameter 2.5 mm and depth 1.5 mm was machined along the implants' vertical axis. The following groups were prepared and characterized: machined implants (M), large grit alumina blasted and acid-etched at high temperature (AE), nanotubular modified by annealing and UV (UvAnNT) and drug-loaded nanotubular (DrNT) surfaces both on dental implants and discs.

The machined (M) implants were used as-machined after cleaning and sterilization without any additional treatment. The acid-etched (AE) implants were grit-blasted with alumina particles with an average size of 250–500 μm and acid etching was done as per previous protocols [29, 30]. For the nanotubular implants, nanotubes were fabricated by electrochemical anodization followed by annealing and UV as per filed patent (Indian Patent Application No: 202111000795). The detailed anodization procedure is explained in section 2.2 of the methodology. Simvastatin drug loading was done just before cell culture experiments and implantation in animals. First, the optimum drug concentration was established through *in vitro* cell culture. Then, drug loading was done through the ultrasonication method as explained in detail in section 2.3. The four groups of implants were packaged in double-sealed bags in a class 1000 clean room facility at the Indian Institute of Technology Delhi, India and Gamma sterilization was carried at Shri Ram Institute of Industrial Research Delhi, India.

2.2. Anodization procedure

Two electrode configurations were used for anodization, as shown in Fig. 1, where the platinum foil acted as a cathode and a dental implant was used as an anode. The distance between the cathode and anode was kept at 4 cm constant for all experiments in the present study. Fig. 1A shows the line diagram of the anodization set up and Fig. 1B shows the anodized animal implants.

In the first step, dental implants and the disc samples were

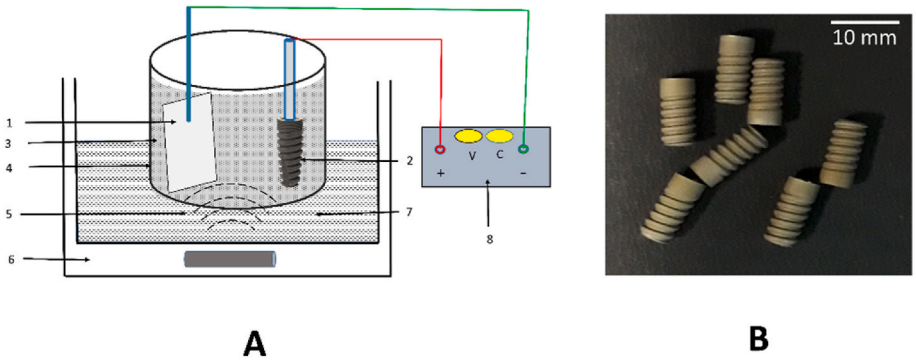

Fig. 1. A. Line diagram of the dental implant anodization setup, B. Dental implants for animal study.(1. Platinum foil cathode, 2. Titanium dental implant anode, 3. Electrolyte, 4. Beaker, 5. Ultrasonic cavitation, 6. Ultrasonic horn, 7. Distilled water, 8. DC power supply).

sandblasted with alumina particles of large grit size (250–500 μm), resulting in roughness (R_a value) of 1.5–2 μm. Implants were ultrasonicated at high frequency to remove grease, dirt, and embedded particles from the implant surface. Then, acid etching was done in a mixture of water (85 vol%), Hydrofluoric acid (HF- 5 vol%) and Nitric acid (10 vol%). It removed the oxide layer and rounded sharp edges resulting from sandblasting. First anodization was done in a viscous electrolyte containing ethylene glycol (96 vol%), ammonium fluoride (0.5 wt%), and water (4 vol%). The process parameters for anodization were optimized to achieve the nanotube diameter in the range of 70–90 nm and a length of 1–1.5 μm over the rough blasted topography. Then, second anodization was done in Fluoride free electrolyte to increase the oxide thickness layer at the base of the nanotubes as explained in the filed patent. Sequential cleaning was done in USP grade acetone (99.9%), absolute alcohol (99–100%), and water (grade 1, high purity), followed by drying in a vacuum oven. Post-anodization annealing was done in the furnace at a temperature of 500 °C in the presence of ambient oxygen with 10 °C per minute heating and cooling rate for 2 h duration. Before characterization, testing, and biocompatibility studies, a 20 min. UV treatment was performed on the surfaces with a UV lamp (15 W, $\lambda = 360 \pm 20$ nm, the intensity of 0.05 mW/cm^2) using a commercially available photo device. Fig. 2 shows the schematics of step by step process of dental implant nanotubular surface modification used in the present study.

2.3. Drug loading methodology

The nanotube surface becomes highly hydrophilic after post-anodization annealing and UV treatment [31]. However, Simvastatin is a water-insoluble drug with an estimated water solubility of 1.45 μg/ml [32]. For loading the drug inside hydrophilic nanotubes, the drug must be hydrophilic. To make the Simvastatin drug hydrophilic, 42 mg of Simvastatin was dissolved in 1 ml of ethanol (95%) and 1.5 ml of NaOH (0.1 M). This solution was heated for 2 h at 50 °C. Neutralization was done with 0.1MHCl to make the final pH 7.2 and deionized water was added to make the final volume 10 ml. This makes the Simvastatin acid of 10 mM concentration which is stored frozen at ¬20 °C.

2.3.1. In vitro assessment of cytotoxic and osteogenic concentrations of Simvastatin drug

Human osteoblast sarcoma cell lines (MG 63) were used to study cytotoxic and osteogenic concentrations of the Simvastatin drug. Procurement of cell lie was done from NCCS Pune, India. Cell lines were cultured in DMEM media with 10% FBS and 1% Penicillin and Streptomycin antibiotics.

Various concentrations of Simvastatin (0.01 μM, 0.1 μM, 1.0 μM, 10 Mm, and 100 μM) were prepared by diluting the stock solution (10 mM Simvastatin) with the culture medium. MG 63 cells were seeded on cell culture disc inside the 24-well plate in a density of 5.000 cells/cm^2 and freshly diluted in culture medium (0.01 μM, 0.1 μM, 1.0 μM, 10 μM and

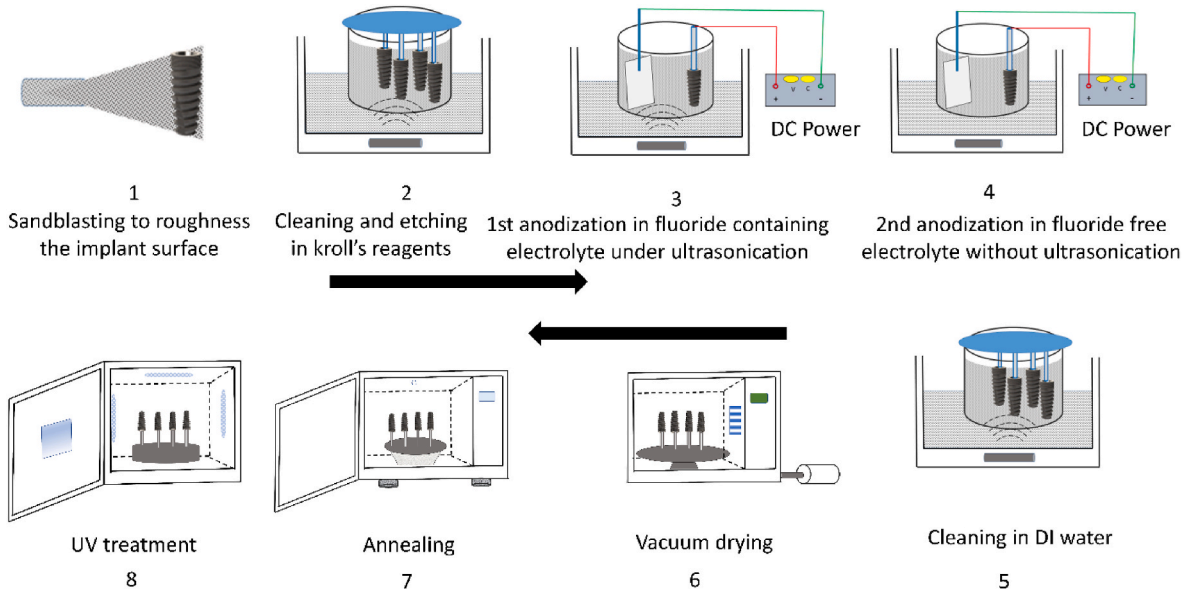

Fig. 2. Schematics showing the steps followed to fabricate nanotubes on the dental implant surface.

100 μM of Simvastatin) was added to each well. Freshly mixed culture medium with Simvastatin was replaced every 3rd day throughout the cell culture study. Cells without Simvastatin in the culture medium were used as a control group. Cell viability and differentiation activity were analyzed at different culture durations. Cell culture was performed with three replicates.

The qualitative assay for cell viability was performed using Calcein/Propidium Iodide (PI) staining after 24 h of cell culture. Calcein (Sigma Aldrich) stained viable cells green, and PI (Fluka, Sigma-Aldrich, Hamburg, Germany) stained nuclei of necrotic and apoptotic cells red. The cells were incubated with 5 μl of 2 mM Calcein in 1 ml of cell culture media for 20 min in the dark. Then, 2.5 μl (1 mg/ml concentration) of propidium iodide (PI) was added and incubated for 10 min. It was washed in PBS and observed under Nikon fluorescent microscope.

MTT assay was done for the 1st, 3rd, and 7th days of cell culture. Commercially available MTT from Sigma was used to study MG 63 cells' proliferation on different titanium surfaces. After each culture period, the discs were rinsed with PBS and incubated with MTT reagent for 4 h in an incubator. There is a purple color formazan crystal formation due to the cleavage of the tetrazolium ring by the mitochondrial dehydrogenase of live cells. After incubation, DMSO was added to dissolve the formazan crystals, and the optical density of the resulting purple solution optical density was measured spectrophotometrically at 574 nm wavelength.

Alkaline Phosphatase Activity (ALP) evaluation was done for the 7th and 14th days. Cells from triplicate samples were washed with PBS. A 500 μl Triton X-100 (0.1% w/v) was added for cell lysis in each well. After that, incubation was done for 2 h in the CO_2 incubator and transferred to a microcentrifuge tube. The cell suspensions were stored at −80 °C till further use. The total protein content was measured by Bradford assay (Bradford protein assay kit, Bio-Rad Laboratories, USA). Crystalline bovine serum albumin (BSA) was used as the standard. A set of standards of BSA were taken and the standard graph was plotted. The protein content of the cell lysate was calculated from this standard graph. Pre-labeled wells of 96-well plates were incubated for 1 h at 37 °C with 100 μL of cell lysate and 100 μL of p-nitrophenol phosphate substrate. 100 μL of 0.3 M NaOH (NaOH; Fisher Scientific Co., USA) stop solution was added. The absorbance of this solution was measured at 450 nm (Biotek Microplate Reader, USA). The alkaline phosphatase activity was expressed as mmoles of p-nitrophenol formed per hour per microgram of protein.

2.3.2. Drug loading by ultrasonic dip-coating method

The loading of the Simvastatin drug inside the nanotube surface was carried out by the dip-coating process. The nanotube implants were soaked in 10 mM Simvastatin solution under ultrasonication for 5 min. Fig. 3 shows the schematics of the drug loading methodology of Simvastatin drug for dental implants. The amount of drug loaded inside the nanotube was determined by Spectrophotometric analysis (by measuring the original and the rinse solutions concentration). The loading efficiency is the percentage of drug-loaded from the drug solution after washing and calculated from the following equation:

$$\eta = \frac{Co - Cr}{Co}$$

where η is the loading efficiency, *Co* is the drug concentration in the original solution, and *Cr* is the drug concentration in the rinse solution.

2.3.3. In vitro drug release

Kinetic release measurements were performed on drug-coated NT discs. Each disc was soaked in a 3 ml phosphate buffer (pH 7.2) in a 24-well plate with orbital shaking at 70 rpm and maintained at 37 °C. 3 ml of the aliquots were sampled periodically for up to 14 days for UV Spectrophotometer analysis. 3 ml of freshly prepared phosphate buffer was added after each sampling for further elution. Simvastatin's cumulative amount was determined with an ultraviolet–visible spectrophotometer (Bio Tek, Power Wave, USA) at λmax 238 nm. The percentage of drug release was calculated by dividing the amount of released drugs by the total drug-loading amount. The total drug-loading amount was the amount of drug released at the end of the experiment when the UV–Vis absorption does not change anymore. For each time interval, three samples were tested, and the mean and the standard deviation of these three samples were used in data analysis. The standard deviation was represented by the error bars in drug release profile graphs.

2.4. Surface characterization

The morphology of the different dental implant surfaces was observed by a field emission scanning electronic microscope (FESEM, JSM-7500F). The roughness was quantified using a 3D optical profilometer (KLE Tencor, Germany).

2.5. Ex vivo mechanical testing of nanotubes in goat jawbone

Ex vivo mechanical testing was done in the goat jaw to test the stability of implant surface coating. For the procedure, the jaw was cleaned with all skin and mucosa, as shown in Fig. 4. Osteotomy holes were prepared sequentially with 2.0, 2.8, and 3.3 mm diameter implant drills at 1200–1500 rpm. Implants were inserted inside the osteotomy using a hand ratchet and removed by reverse torque. The removed implant surface was analyzed visually and under a scanning electron microscope for the nanotube coating stability.

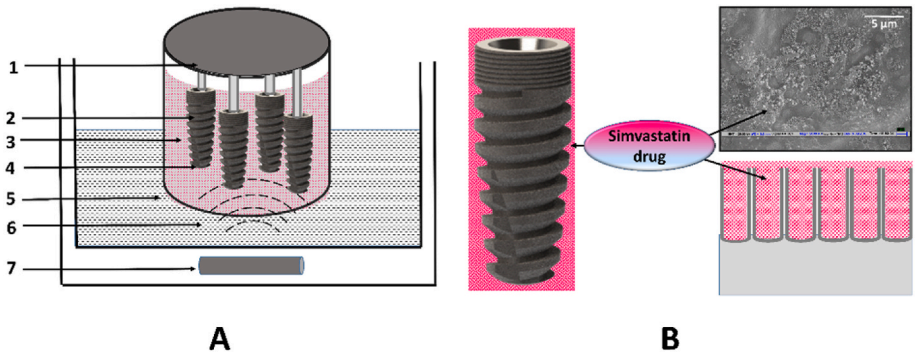

Fig. 3. Drug loading methodology A. Dipping of the implant in drug under ultrasonication B. FESEM image showing drug loaded surface (upper right) schematics of the loaded drug inside nanotube (lower right). (1. Implant holder, 2. Dental implants, 3. Simvastatin drug solution 4. Nanotube surface, 5. Distilled water, 6. Ultrasonic cavitation, 7. Ultrasonic horn).

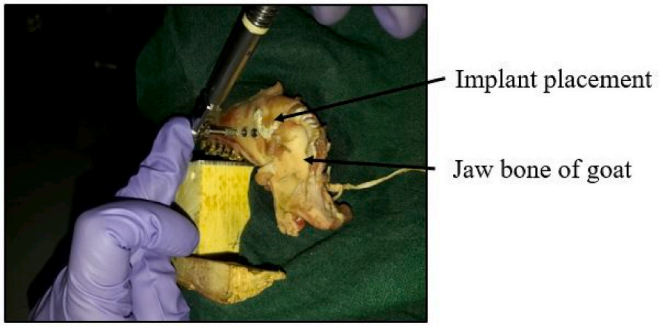

Fig. 4. *Ex vivo* mechanical testing of nanotube dental implants in the fresh jaw bone of a goat.

2.6. In vitro cytocompatibility assessment on disc samples

Human osteoblast sarcoma cell lines (MG-63) were used to study cell adhesion, proliferation differentiation, and mineralization activity on different experimental surfaces. Disc samples of 5 mm diameter with machined, acid etched, nanotube, and drug-loaded nanotube surfaces were used for this study. Cells were seeded on a titanium disc with 5000 cells/cm^2 density and media was put on the seeded sample after 4 h so that the cells can adhere to the samples. Media was changed every 3rd day and cell culture was done for a different duration as per the type of assays and staining.

FESEM evaluation of cell adhesion and morphology was done after 48 h of the cell culture period. The disc samples were fixed with 4% formaldehyde after 48 h of culture and then sequentially dehydrated in a series of alcohol (50–100%). After gold sputter coating FESEM was used to evaluate cell adhesion and proliferation on the disc surface. Immunofluorescence staining with Rhodamine-Phalloidin and DAPI was done 48 h after cell culture. Disc samples were washed with PBS and then fixed with 4% formaldehyde for 20 min. Samples were again washed with PBS and blocked with the 1% BSA solution for 1 h and then disc samples were again washed with PBS and stained with Rhodamine-Phalloidin for 20 min and DAPI for 5 min. Cell morphology was then seen in the Nikon fluorescent microscope.

Live and dead cell staining was done with Calcein green and Propidium Iodide (PI) after 24 h of culture duration and evaluation was done under the fluorescent microscope following staining. MTT assay was done for the 1st, 3rd, and 7th days of cell culture on disc samples of each experimental surface. The alkaline phosphatase test estimated cell differentiation activity on the 7th and 14th day of cell culture. The mineralization activity was evaluated by the colorimetric quantification of calcium. The Alizarin red S (ARS) staining was performed on the 14th and 21st days. First, samples were washed with sterilized and filtered PBS. Fixation was done with 4% paraformaldehyde for 25 min. Then samples were rinsed 3 times with distilled. A 40 mM Alizarin stain at 4.1 pH was added to the fixed cells for 20 min. This produces a red complex via a reaction with calcium. The fixed and stained cells were incubated with 200 μL of 10% acetic acid for 30 min. After incubation, the adhered cells were scraped and the mixed solution was transferred to a microcentrifuge tube for heating for 10 min at 80 °C temperature. After heating, the cells were centrifuged and the supernatant solution was transferred to a new tube. 10% ammonium hydroxide was added to neutralize the residual acid. The absorbance was measured at 405 nm by the microplate reader.

2.7. In vivo procedure methodology

2.7.1. Animal surgery and care

Twelve New Zealand white rabbits of 3–5 kg in weight were used in this study. This investigation followed all the institutional ethical guidelines (Guide for the Care and Use of Laboratory Animals) for the protection of animals and ethical approval for animal experimentation was taken from an ethical committee, All India Institute of Medical Sciences, New Delhi *(Ethical Clearance no. 25/IACE-1/2017)*. The housing of rabbits was done individually inside stainless-steel cages in the designated animal room, where the temperature was controlled. As per Table 1, rabbits were divided into four groups randomly. Under the aseptic condition, all the surgical procedures were performed inside the designated minor operation theatre area. Seventy-two threaded dental implants (Φ3.5 × 8 mm) were prepared as described above. A total of 18 implants were used per group for the *in vivo* studies.

Ketamine at a dose of 30 mg/kg body weight was used to anesthetize the rabbit by intramuscular injection. The skin of rabbits was shaved and scrubbed with 2% povidone-iodine to provide a clean and sterile surgical field prior to surgery. Approximately, a 2 cm long incision was made on the tibia's medial-proximal aspect below the knee joint. Subperiosteally, the flap was raised with the help of a periosteal elevator to expose the bone. A guide drill of 1.8 mm diameter was used to drill the pilot osteotomy hole inside the cortical bone using a slow-speed handpiece (>2000 rpm) along with copious saline irrigation. After the guide drill, a 2 mm first drill followed by a 3.3 mm final drill was used sequentially. The implants were installed with NSK Surgical physiodispensor with 20:1 torque reduction handpiece (NSK, Germany) and insertion torque was measured at the same time. Fig. 5, depicts the surgical armamentarium and procure in step by step manner.

Each rabbit received a total of 6 implants 3 per tibiae. Each group implant was placed in 3 rabbits for the triplication of the study. After the insertion of the implant into the holes, primary closure was achieved for each animal by layered suturing. All rabbits recovered from the surgery within 1–2 h and displayed normal activity as well as mobility. After surgery, the rabbits received antibiotics for 3 days and were allowed to bear full weight. The animals were sacrificed as per the animal ethical committee guidelines with an overdose of sodium pentobarbital (10 ml of 100 mg/ml) after 4 weeks. The implant samples were harvested along with tibias after stripping the overlying soft tissues. Half samples were used for reverse torque removal testing immediately, while half were rinsed in saline and preserved in 10% buffered formalin for micro-CT and histopathological examination.

2.7.2. Reverse torque removal test

The bone and soft tissues from the top of dental implants were removed carefully before the test. A total of 36 samples (9 from each group) were tested. A special fixture was fabricated for reverse torque testing Fig. 6A (a&b). This fixture was connected to the force Dynamometer (Kistler) at the base. Then the implant with the bone block fastened inside the fixture and the implant was removed (Fig. 6 A-c) from the bone after applying reverse torque using a torque ratchet and implant driver. The dynamometer recorded the maximum torque used for the removal of the implant in N-cm.

2.7.3. Micro-CT analysis

The bone formations around the different experimental dental implants were examined three-dimensionally (3D) using micro-computed tomography (μCT 50, Scanco Medical, Basserdorf, Germany). Five hundred μCT slices with a slice resolution of 36 μm were imaged (X-ray

Table 1
Study design; distribution of implants in experimental and control groups.

Group	Surface	Total no of implants per rabbit X no. of Rabbits (total implants in each group)
Group 1	Machined	6x3 (18)
Group 2	Acid-etched	6x3 (18)
Group 3	Nanotube	6x3 (18)
Group 4	Drug loaded nanotube	6x3 (18)

Fig. 5. The procedure followed for animal surgery A & B. Instruments Set up, C. Rabbit model, D. Anesthesia, E. Incision, F. Drilling sequence, G. Osteotomy prepared, H. Implant placement, I. Suture placement.

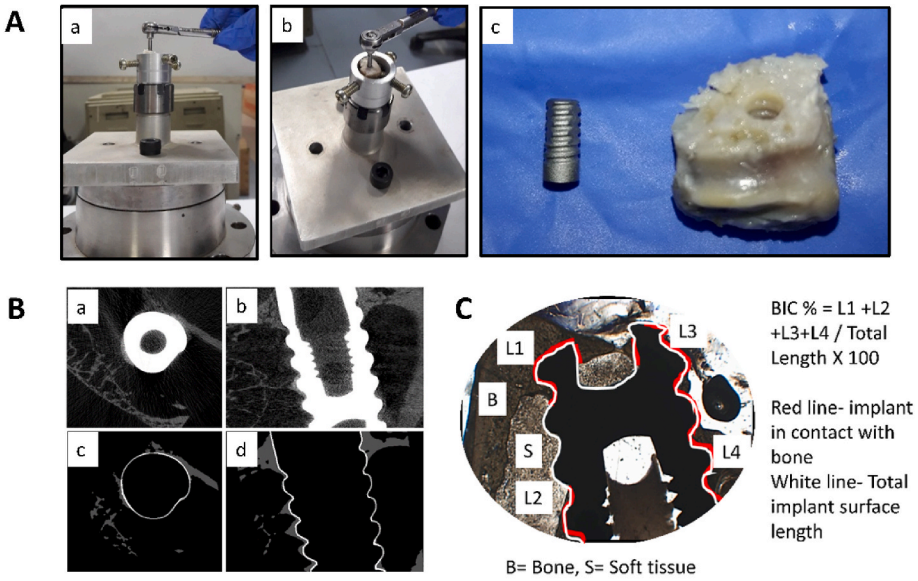

Fig. 6. A. Reverse torque removal a&b) Setup c) Removed implant and bone sample B. ROI assessment for BV% (bone volume) calculation in Micro-CT evaluation C. BIC % calculation on histopathology images using Image J software (L- length, B- bone, S- soft tissue).

energy of 55 kV, and a current of 145 μA). The integration time was about 200 ms resulting in a total scanning time of 36.3 min. The inbuilt software analyzed the data. Since, in some cases, the coronal part of the dental implant was outside the bone, the data was cropped till where the bone started. Segmentation was done after determining the threshold levels for bone and implant (based on the grey-scale histogram and visual inspection).

After segmentation, a 0.75 mm region of interest (ROI) was defined, from where the bone volume (BV) would be calculated, as shown in Fig. 6B. Subsequently, bone and implant in the ROI were differentiated, creating the three volumes, i.e. bone, implant and soft tissue or empty space, based on their respective threshold values and converted into a tetrahedral grid hence volume measurement was possible.

2.7.4. Histological procedure

The fixed specimens were dehydrated in the increasing concentration of ethanol (70–100%), cleared using the acetone-alcohol mixture, and then embedded in the methylmethacrylate (MMA) resin. After polymerization in MMA, thick sections were cut from the PMMA block (70–100 μm) using a linear precision saw microtome (ACCUTOME 100 Struers, Denmark). These sections were stuck to a glass slide, grounded and the surface was polished using a variable speed grinder polisher (ECOMET 3000, Buehler, Germany) to a final thickness of 40 μm. Then staining was done with hot Stevenel's blue and Van Gieson's picrofuschin. The stained sections were evaluated in a trinocular transmitted light microscope (Nikon E600) and photomicrographs were captured using the camera (Nikon DS Ril) attached to the microscope. The histomorphometric data was analyzed by image analysis software (Image J 1.5 0i/java 1.8; National Institutes of Health) as shown in Fig. 6C. Bone-Implant contact (BIC) percentage was calculated along with the entire implant with 10 Xobjective magnification.

2.8. In vivo mechanical performance evaluation of nanotubes after reverse torque removal

After reverse torque removal, the removed dental implants of the

nanotube group were evaluated for the integrity of the nanotube surface. Fig. 6A–c shows the representative images of the removed implant and bone. The nanotubular and drug-loaded nanotubular dental implants were evaluated by a field emission scanning electronic microscope (FESEM, JSM-7500F) after removal from the bone. They were immediately dehydrated in a series of alcohol (50–100%) and gold-sputtered before FESEM evaluation. The bone was demineralized, dehydrated, embedded, and sectioned. Sections were stained with Hematoxylin and Eosin (H&E) to evaluate the local toxicity of nanotubes.

2.9. Systemic toxicity evaluation of the nanotube implants in vivo on different organs

At 4 weeks, when animals were sacrificed, the main organs (liver, lung, spleen heart, and kidney) were dissected immediately and placed in 4% neutral buffered formalin solution for 48 h. After fixing, dehydration was done with a series of graded ethanol solutions (70.0–99.8%), cleared in xylene, and embedded in wax paraffin. Further, 4 μm thick sections were prepared with a microtome (Leica RM 2255, Germany). The sections were then stained with H&E. For the histopathological analysis, the slides were examined blinded, and photographed under a trinocular transmitted light microscope (Nikon E600).

2.10. Statistical analysis

For the determination of significant differences among the various experimental and control groups, data were subjected to two-way ANOVA (Analysis of Variance) using Origin Software. The significance was determined at a 95% confidence level. The average data were presented with standard deviation and *p-value>0.05 was considered significant. The number of samples for each group per test per time point was 3.

3. Results

3.1. In vitro assessment of cytotoxic and osteogenic concentrations of Simvastatin drug

Fig. 7A–E shows the confocal images of cells stained by live and dead cell stains to determine the cytotoxicity of different drug concentrations. Simvastatin concentrations of 10 μM and 100 μM showed marked cytotoxic effects as evidenced by dead cells stained red. The surviving cells (stained green) at these concentrations displayed a change in morphology which is more elongated and spread (Fig. 7E&F). According to the results, the highest Simvastatin concentration was 1.0 μM, showing no dead cells (Fig. 7D). On the contrary, 0.1 μM and 0.01 μM Simvastatin concentrations showed enhanced proliferation (more no of cells) compared to the control whereas, 0.1 μM and 1.0 μM Simvastatin concentrations showed a spread type of cell morphology. 1.0 μM Simvastatin concentration displayed increased numbers of filopodia and lamellipodia on 1st day of cell culture suggesting a differentiated morphology of cells (Fig. 7D).

Fig. 7G showed the proliferation of cells in different concentrations of Simvastatin drugs by the MTT assay method. On day 1st, there was decreased proliferation of cells in the case of 1.0 μM, 10 μM, and 100 μM Simvastatin concentrations compared to the control whereas, 0.1 μM and 0.01 μM Simvastatin concentrations showed enhanced cell

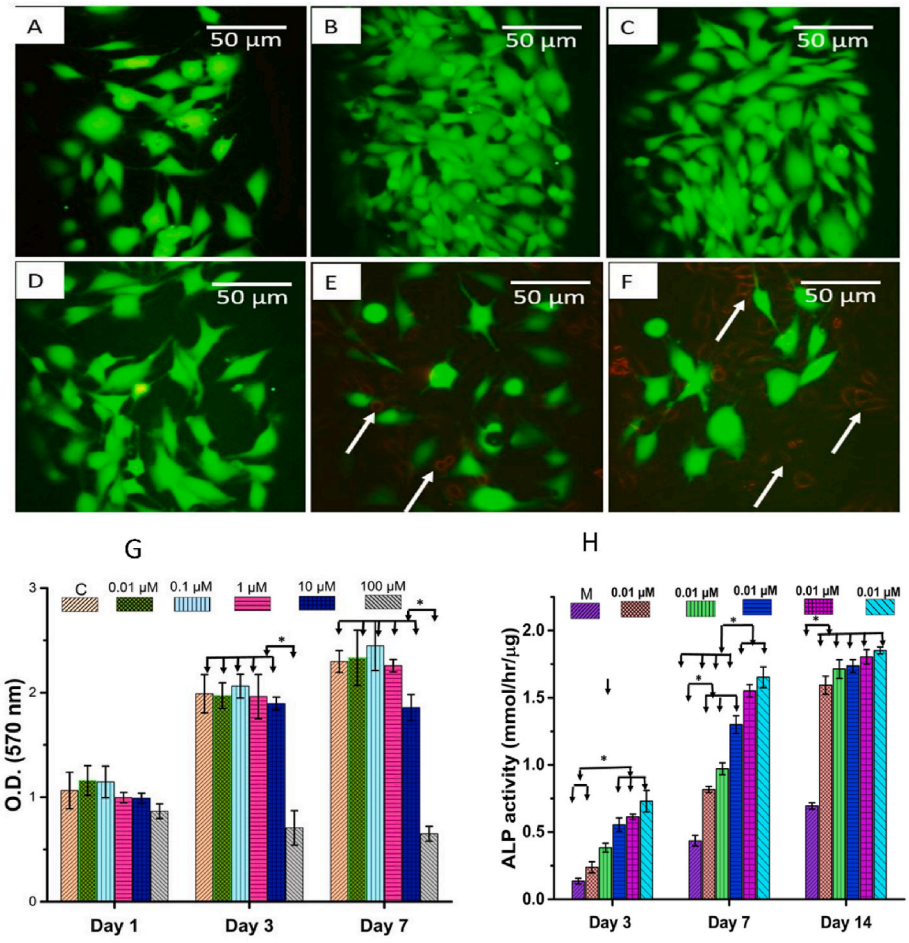

Fig. 7. Confocal images of MG-63 cells after live and dead cell staining by Calcein green and PI (Propidium Iodide) cultured with different concentrations of Simvastatin A)Control, B)0.01 μM Simvastatin, C)0.1 μM Simvastatin, D)1.0 μM Simvastatin, E)10 μM Simvastatin, and F)100 μM Simvastatin (arrow showing dead cells) G)Bar graph showing the optical density of the cell culture treated with different concentrations of Simvastatin at day 1st, 3rd and 7th using MTT assay. H)Bar graph showing mineralization activity of MG-63 cell treated with different concentrations of Simvastatin after 3rd, 7th, and 14th days of cell culture, *p-value< 0.05 and n = 3 for each concentration and time point.

proliferation as evidenced by increased OD. On day 3rd, 10 μM and 100 μM Simvastatin showed a significant decrease ($p < 0.05$) in the MG 63 cells' viability compared to the other Simvastatin concentrations and the control group. Day 7th culture also showed a significant decrease ($p < 0.05$) in the viability of the MG 63 cells with the 10 and 100 μM Simvastatin concentrations compared to the 0.01 μM, 0.1 μM, 1.0 μM Simvastatin concentrations, and the control group. At Simvastatin concentration higher than 10 μM, cells' viability was inversely proportional to the drug concentration and time. Simvastatin concentrations of 0.1 μM exerted the most pronounced effect on proliferation.

Fig. 7H shows Simvastatin's effect on osteoblast differentiation evaluated by quantitative colorimetric ALP assay at 3rd, 7th and 14th days. On 3rd day, the 1.0 μM, 10 μM, and 100 μM Simvastatin concentrations showed significantly increased ALP activity ($p < 0.05$). There was almost 3-4-fold increased ALP activity at 10 μM and 100 μM Simvastatin concentration. On the 7th day, the same trend of increase in ALP activity was observed. However, at this time point, 0.01 μM and 0.1 μM Simvastatin concentrations also showed a significant increase in ALP activity compared to the control. At 14th days, all Simvastatin concentrations exhibited nearly similar ALP activity and it was significantly higher than the control group. Thus Simvastatin showed the increased ALP activities directly proportional to the different concentrations and at every investigated time point. However, on day 14th, all concentrations of Simvastatin exhibited nearly similar ALP activity.

The optimized drug concentration from *in vitro* cell culture assessment method was in the range of 0.01 μM and 1 μM.

3.2. In vitro drug loading and release from drug-loaded implant samples

An *In vitro* Simvastatin release study from a drug-loaded NT disc was performed in PBS of 7.3 pH at 37 °C. Fig. 8A shows the calibration curve of the Simvastatin drug at λ_{max} 238 nm. The drug loading efficiency was 57.14% under the ultrasonication dip coating. A total of 24 μg of the drug was loaded per implant. The release profiles of Simvastatin from drug-loaded NT samples are shown in Fig. 8B. It showed a typical two-phase release profile, which indicates a relatively rapid initial release of the drug, followed by a sustained and slow release of the drug over a prolonged period. Around 40% of the drug was released on day 1 and the remaining drug was released over 13 days. A total cumulative release of 24 μg was detected in 14 days, including the first day's burst release.

3.3. Surface characterization

Fig. 9A shows the FESEM images of the machined, acid-etched, nanotube, and drug-loaded nanotube surfaces. The machined surface displays grooves of machining and otherwise, it is smooth. Acid-etched surfaces have rough and porous topography. The nanotube surface shows uniformly formed nanotubes on rough surfaces and the diameter of the nanotubes is nearly 80 nm. On the drug-loaded nanotube surface, the rough topography has retained a certain amount of drug and the nanotube mouth can't be observed in certain places. However, there is no gross difference in topography on the nanotube and drug-loaded nanotube surfaces. Fig. 9B shows the average roughness of these different surfaces. The machined surface is the least rough while the average surface roughness of acid-etched and nanotube surfaces is in the range of 1.5–2 μm as represented in Fig. 9B.

3.4. Ex vivo mechanical testing of nanotubes in goat jawbone

After the removal of the nanotube dental implant from the goat jaw bone, the surface was inspected visually as well as by FESEM for any delamination. No plastic deformation/delamination was observed of the nanotube implant surface after insertion and reverse torque removal from the bone. Fig. 10A shows the photograph of the nanotube dental implant before insertion and Fig. 10B shows the removed nanotube dental implant from bone. There is no delamination of the nanotube layer from the anodized nanotube dental implant surface. Fig. 10C&D shows the morphology of the nanotube dental implant surface before insertion and after removal from the bone. In both cases, nanotubes are present uniformly over the surface and there is no deformation or delamination of the nanotubes. This finding suggests that the integrity of the titanium nanotube on the dental implant surface remained intact during its insertion and removal.

3.5. In vitro cytocompatibility assessment on disc samples

3.5.1. Cell morphology by FESEM imaging

Fig. 11A shows FESEM images of cells adhered to the different nanotube surfaces after 48 h of cell culture. Analysis of the micrographs revealed a difference in cell density and cell morphology on different surfaces. Cell density was greatest on UvAnNT samples followed by DrNT and AE surfaces. Cell filopodia were not visible on the machined surface, whereas small filopodial extensions were clearly visible at the cell periphery in the case of the acid-etched surface. In contrast, UvAnNT & DrNT surfaces showed cell spreading with elongated filopodial and lamellipodial extensions on the surface of the nanotube. Cells adhered on UvAnNT samples showed stretching in one direction with longer lamellipodia, whereas cells on the DrNT samples surface showed more or less uniform spreading in all directions with greater inter-cell communications. The visual inspection gives an impression that the cells cultured on UvAnNT & DrNT surfaces have the highest cell density of adhered cells and a relatively greater number of filopodial extensions. DrNT surfaces displayed maximum cell spreading and inter cells communications.

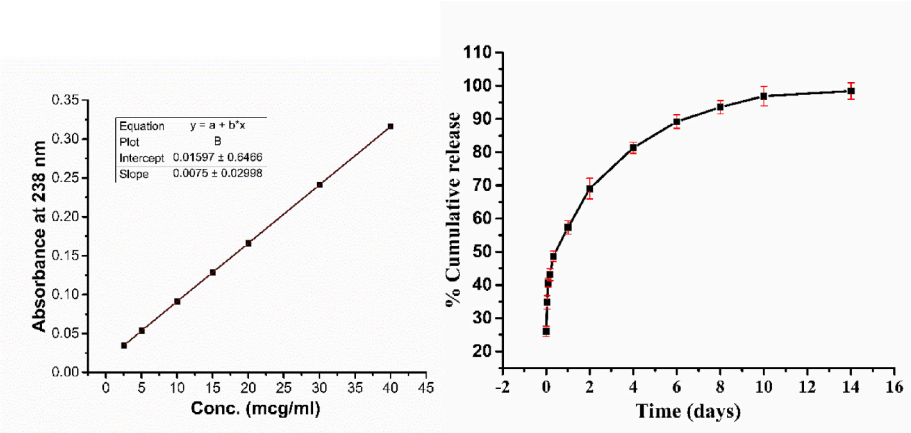

Fig. 8. A. Calibration curve B. Drug release profile.

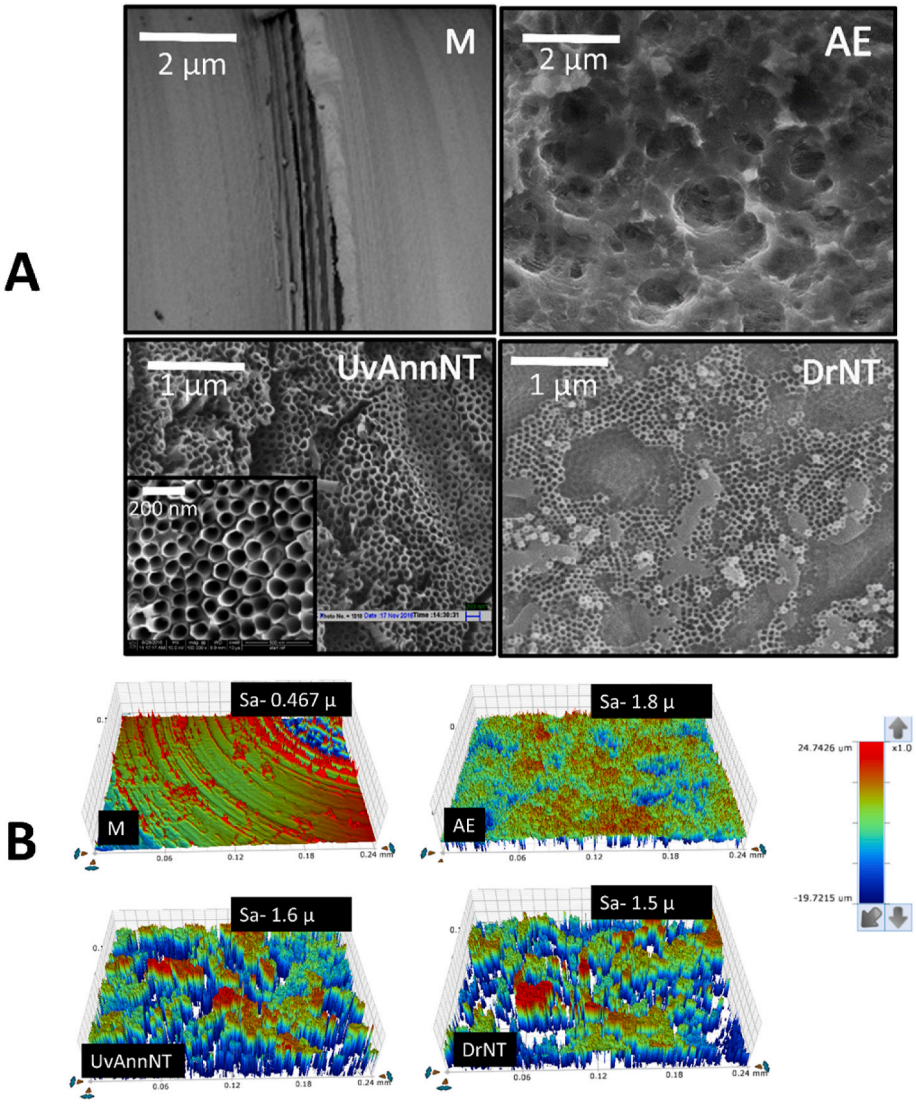

Fig. 9. A. FESEM images of different implant surfaces (M-machined, AE-Acid etched, UVAnnNT- Nanotube surface, DrNT- Drug loaded surface, B. 3D optical images showing the topography and average roughness of different surfaces.

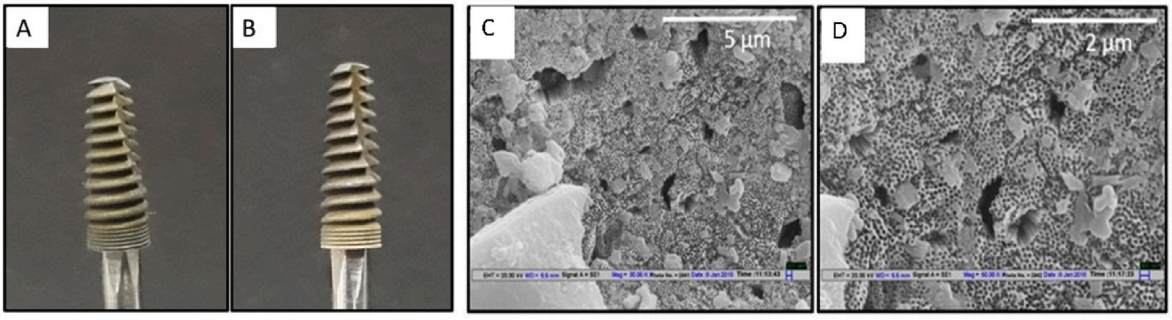

Fig. 10. A& B Implant photographs before insertion and after insertion plus removal, C&D SEM image of implant surface before insertion and after insertion and removal from the jaw bone of goat.

3.5.2. Cell cytoskeletal morphology by immunofluorescence staining

Fig. 11B shows the confocal images of adhered MG 63 cells on different surfaces after 48 h of cell culture. Machined and acid-etched surfaces displayed rounded to polygonal cell morphology; however, filopodial extensions were observed on the AE sample surface. The distribution pattern of the actin filaments appeared to be diffused on the machined surface. DrNT & UvAnNT samples displayed elongated cell morphology along with a highly organized pattern of actin filaments.

3.5.3. Estimation of cell proliferation and viability by live and dead cell staining

Fig. 11C shows the fluorescent images of live and dead after 24 h of cell culture on control and experimental surfaces. No dead cells were observed on the samples; however, a difference in cell density and morphology was observed. Cell density was highest on UvAnNT samples followed by DrNT > AE > M surfaces. These results are similar to the FESEM results. Cell morphology also appears to be more spread and

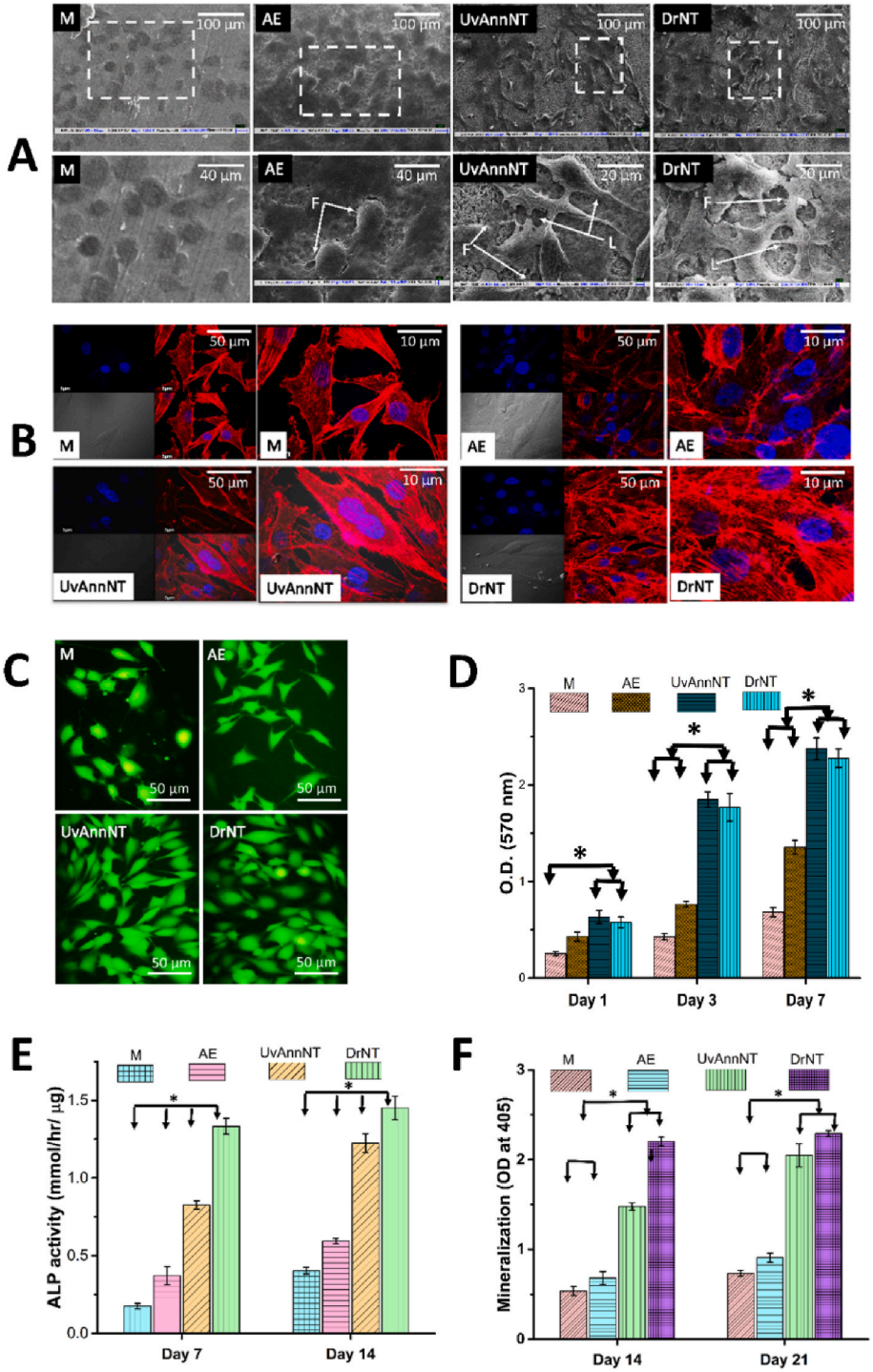

Fig. 11. A. FESEM images of MG 63 cells adhere to the different surfaces at low and high magnifications after 48 h of cell culture, B. Fluorescent images of MG 63 cells stained with Rhodamine-Phalloidin and DAPI on the different surfaces at 48 h of cell culture, C. Live, and Dead cells on surfaces stained with Calcein Green and Propidium Iodide at 48 h of cell culture D. MTT assay graph showing the optical density of cells on different surfaces at 1st, 3rd and 7th days. E. Graph showing ALP activity on different surfaces at 7th and 14th days, F. Graph showing mineralization activity estimated by alizarin assay at 14th and 21st days of cell culture*p value < 0.05 and $n = 3$ for each concentration and time point.

elongated on DrNT & UvAnNT samples.

3.5.4. Estimation of cell proliferation by MTT assay

Fig. 11D shows the optical density (OD) of the MTT assay representing the cell proliferation index of different control and experimental surfaces. On day 1st, the UvAnNT showed the highest proliferation, followed by DrNT > AE > M surface. This difference was statistically significant for UvAnNT vs M and DrNT vs M surfaces at the p-value <0.05. On the 3rd and 7th days, similar trends of cell proliferation were observed. However, at these time points, the difference was also significant between DrNT vs AE and UvAnNT vs AE surfaces. The increased OD on DrNT & UvAnNT samples can be attributed to the increased number of cell adhesion and proliferation. The proliferation of cells on drug-loaded nanotube samples was comparable to the nanotube samples without the drug, thus indicating the non-cytotoxic level of the Simvastatin drug was released *in vitro*.

3.5.5. Estimation of ALP activity

The normalized ALP activity of MG-63 cells over different sample surfaces is shown in Fig. 11E after the 7th and 14th days of cell culture. There was a statistically significant difference in the normalized activity of ALP between all surfaces at both observation time points.

3.5.6. Estimation of mineralization activity

The mineralization activity of MG 63 cells on different samples estimated by alizarin assay are shown in Fig. 11F on the 14th and 21st day of cell culture. On days 14th and 21st, the UvAnNT and DrNT sample surfaces showed a statistically significant increase in mineralization activity than AE & M surfaces. Although the activity on DrNT was also higher than the UvAnNT surface at both time points, the result was statistically significant on day 14th and insignificant on day 21st (p-value <0.05). This observation suggests that the drug-loaded surface leads to early mineralization.

3.6. In vivo result

All the animals recovered quickly from implant surgery, and neither clinical signs of inflammation nor infections were observed. All types of implants appeared well integrated into the bone after 4 weeks without macroscopic signs of osteolysis.

3.6.1. Reverse torque removal

Fig. 12A shows the bar diagram, showing the maximum torque value of removal for different surface implants after 4 weeks of healing. The highest torque was required by the drug-loaded surface whereas the machined surface required the least torque. There is a statistically significant difference in reverse torque removal between each group (p-value <0.05).

3.6.2. Micro-CT analysis

Fig. 12B shows the 3D reconstructive micro-CT images of experimental and control implants with the surrounding bone. It can be observed that the bone volume around the DrNT implant was very high compared to all other surfaces. The bone was observed inside the groove area and a very few/scanty bone trabeculae on the machined implant. On the AE surface also there was partial bone apposition on the implant surface. However, the amount of bone was higher than the machined one. Although all surface was covered with the bone on the UvAnNT implant, the thickness and density of trabeculae were less compared to the DrNT implants.

In Fig. 12C, the bar diagram shows the bone volume percentage (BV %) around the control and experimental implant surface. It has been observed that the DrNT implant surface shows the highest bone volume, followed by nanotube surfaces. The machined implant showed the least BV%, followed by AE. The BV% difference was statistically significant among all groups (p-value<0.05).

3.6.3. Histopathological analysis

All the animals recovered quickly from implant surgery, and neither clinical signs of inflammation nor infections were observed. All types of implants appeared well integrated into the bone after 4 weeks without macroscopic signs of osteolysis.

Qualitative evaluation of the histological section, as shown in Fig. 13A, B & C, revealed new bone formation around the dental implants of all surfaces. However, gaps can be observed between the M & AE implant surfaces and newly formed bone. On the machined implant surface, a connective tissue layer was also seen to be interposed between the newly formed bone and implant surface (Fig. 13A and C) while there is direct apposition of new bone on the implant surface without intervening gaps on UvAnnNT and DrNT implant surface. AE surface showed partial apposition of bone as compared to machined surfaces. Mineralized bone trabeculae were observed in the peri-implant region of the different surface implants. Thin trabeculae (characteristic of newly formed bone) were visible around the implants in the case of M and AE surfaces, whereas they are thicker on UvAnNT and DrNT implant surfaces (Fig. 13C). In the apical bone growth chamber (Fig. 13B) of the UvAnNT and DrNT implants, the abundant newly formed woven bone was observed while no bone was seen in the AE and M implants.

Quantitative assessment of the bone-implant contact percentage (BIC) on different dental implant surfaces is shown in Fig. 13D. There was a statistically significant difference between all the groups, i.e. machined, acid-etched, and nano-surface implants. The quantity of bone was three times on the nanotube and four times on drug-loaded nanotubes as compared to the machined surface. It was found to double on the drug-loaded nanotube surface as compared to the acid-etched surface.

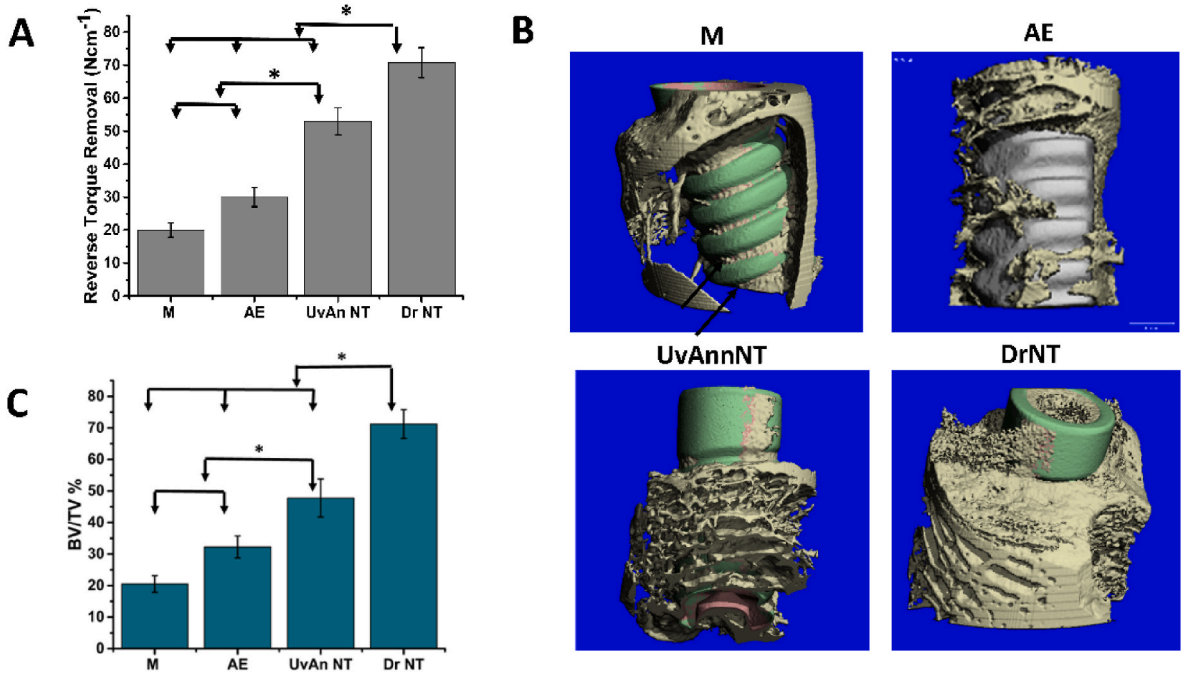

Fig. 12. A. Reverse torque removal set up and removed the implant from the bone, B. Bar diagram showing reverse torque removal (in N-cm) of different implants from the bone after 4 weeks of healing *p-value < 0.05 and n = 9 for each surface, C. 3-D reconstructed images of machined, Acid etched, Nanotube & Drug loaded implants and surrounding bone at 4 weeks of healing, D. Bone volume (BV) percentage around different Implant surfaces, *p-value < 0.05 and n = 9 for each surface.

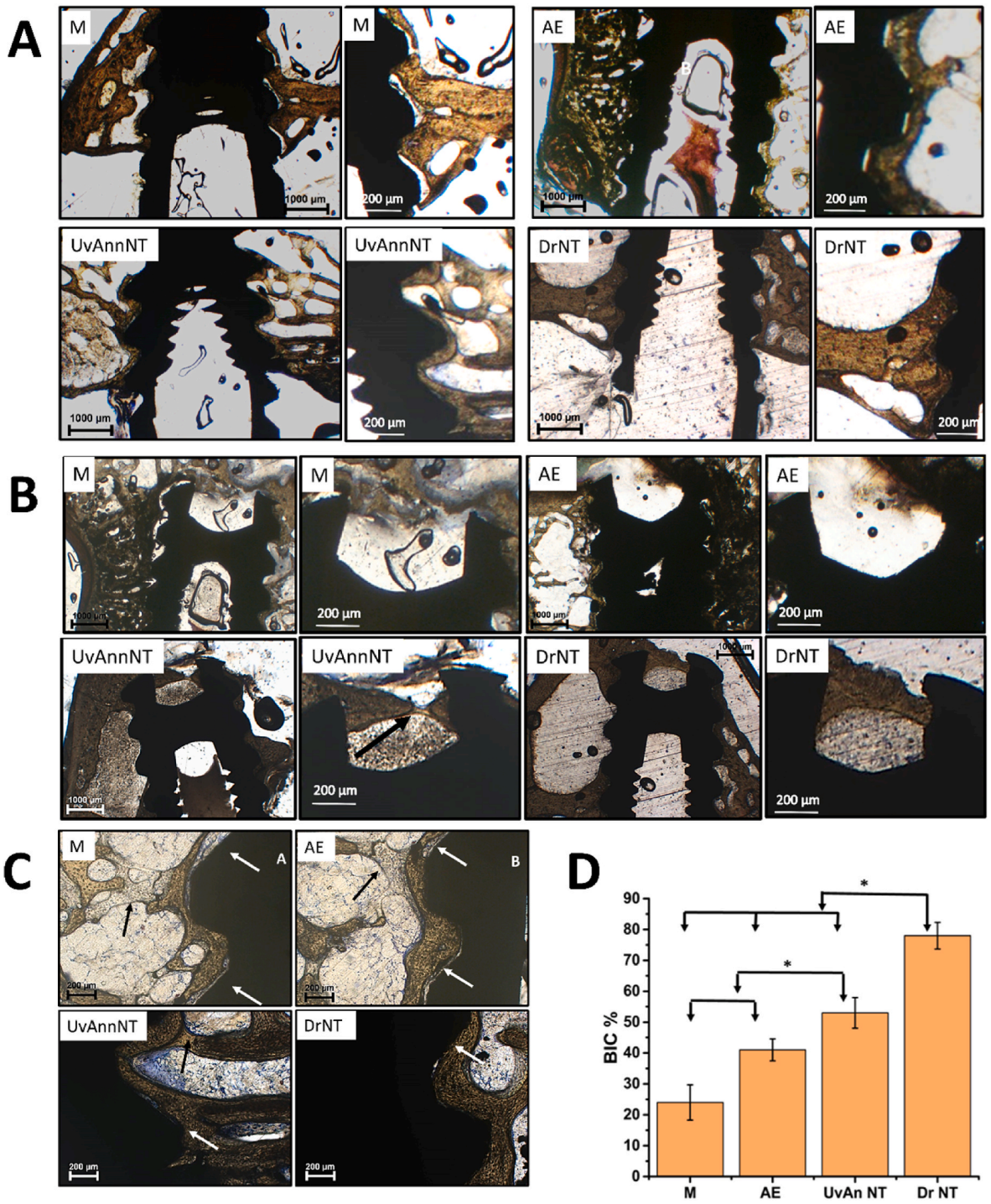

Fig. 13. A. Histopathological images of different surface implant and bone interface, B. Histopathological images of implant and bone interface showing bone growth inside the apical chamber of the implant, C. Histopathological images of implant and bone interface showing bone growth inside threads of the implant, D. Bar graph showing Bone implant contact (BIC) percentage around different Implant surfaces *p value < 0.05 and $n = 9$ for each surface.

3.6.4. In vivo mechanical performance evaluation of nanotubes after reverse torque removal

Fig. 14 shows the nanotubes and drug-loaded nanotube dental surfaces after removal from the bone by reverse torque method at lower and higher magnifications. Bone tissue can be observed inside the thread portion of the dental implant in Fig. 14A&B. There is no gross delamination of nanotubes. Nanotubes can be clearly observed in between bone deposition areas on both nanotube and drug-loaded nanotube dental implant surfaces (Fig. 14C&D). There is no gross deformation or change in the morphology of the nanotube over the dental implant surfaces in both cases.

3.6.5. Systemic and local toxicity evaluation of the nanotube implants in vivo on different organs

Fig. 15 shows the representative histopathology photographs of the bone tissue around implants and different main organs (liver, kidney, heart, lung, and spleen). There were no gross pathological changes (ex. deformation, necrosis, or atrophy) observed in the main organs during dissection and grossing. The cell morphology and tissue architecture of each examined organ appear normal and similar to control machined implants.

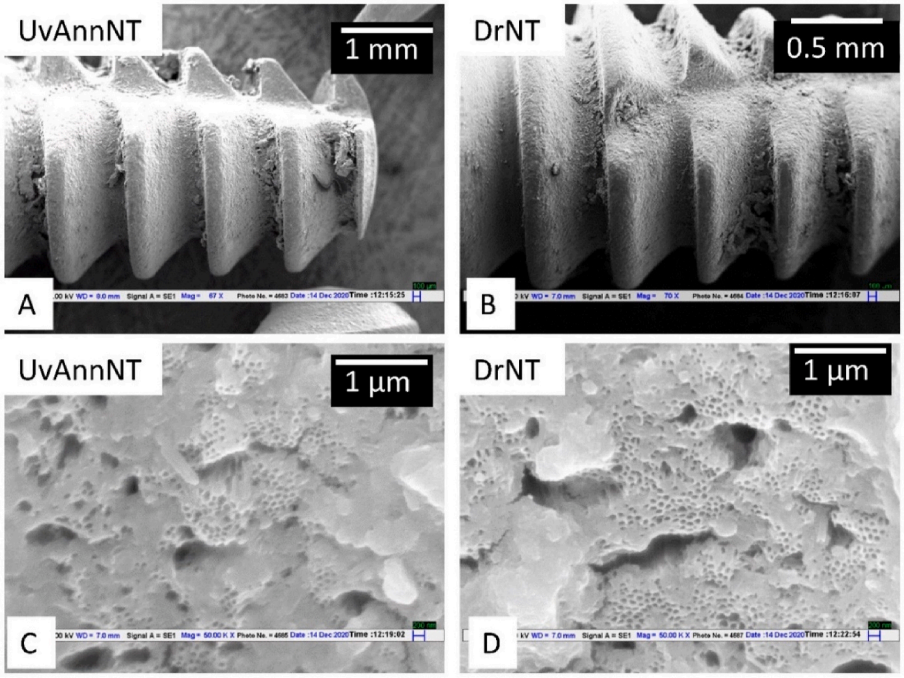

Fig. 14. FESEM images of A&C) Nanotubular dental implants B&D) Drug-loaded nanotubular dental implant after removal from rabbit bones by reverse torque testing.

3.6.5.1. Liver. The histomorphology of the liver was very similar in animals from all groups (Fig. 15 A, B&C). The classic lobules (defined as polygonal structures with several portal tracts at the periphery and a central vein in the center) were observed in all implant groups of animals (Fig. 15A). There was no abnormality in hepatocyte cell morphology and arrangement in columns, liver sinusoids/capillaries of the liver. No necrosis was observed and no megakaryocytic cells/inflammatory were seen in the animals.

3.6.5.2. Kidney. In the kidneys, normal glomerular and tubular histology was observed in animals of both control and nanotube group animals (Fig. 15D, E&F). There was no hyperemia and tubular edema observed in any group of animals. No inflammatory cells or necrosis were seen.

3.6.5.3. Heart. The Photomicrographs of H&E stained sections (Fig. 15 G, H&I) of myocardial tissue revealed that myocardial cytoplasm and nuclei were clear and well distributed. In all groups, cardiomyocytes with eosinophilic cytoplasm were observed and most muscular cells were oriented longitudinally, and the faint cross-striations are evident. Between cardiomyocytes loose connective tissue containing fibroblasts was also observed in all group animals. No visible hyperemia or necrosis occurred in the animals of all groups.

3.6.5.4. Spleen. Histopathologically spleen is divided into white and red pulp. White pulp consists of a cylindrical mass of lymphocytes arranged around a central artery and red pulp consists of splenic sinuses surrounded by splenic cords as observed in Fig. 15 J, K&L. There is no difference observed between the control and nanotube implant. No megakaryocytic hyperplasia was observed in the red pulp of the nanotube groups. Splenic parenchyma of red pulp is also normal without any hyperemia/hemorrhage. Moreover, the volume distribution of both white and red pulp is nearly similar in all groups.

3.6.5.5. Lung. No morphological alterations were found in the lungs of the control and nanotube implants animal group. Fig. 15M, N&O shows photomicrographs of an intrapulmonary bronchiole, lined with columnar to cuboidal epithelium with some ciliated cells.

3.6.5.6. Local toxicity on bone. Both cortical and cancellous bone was seen in the sections of bone which were harvested around the implants after reverse torque removal of implants. The chronic inflammatory cells infiltrate (Lymphocytes, macrophage, and giant cells) were not seen in all groups. The differentiated capillary vascularization was observed in between trabecular spaces. No evidence of bone necrosis or fibrous capsule was present in any of the implant group animals.

4. Discussion

Earlier research has also established that the surface topography of titanium influences the proliferation and differentiation of osteogenic cells [33]. However, in the present research, the differentiation and mineralization activity was compared on the machined, acid-etched, nanotube, and drug-loaded nanotube surfaces and the result was found to be statistically significant. The drug-loaded nanotubular surface showed early differentiation (1 week) and mineralization activity (2 weeks) as compared to the nanotube surface. It was also observed that the Simvastatin drug-loaded samples showed cell adhesion, viability, and proliferation similar to that of the nanotube surface along with early differentiation and mineralization capability, hence concluding that the drug released from the nanotube surface is capable of inducing early osteogenesis.

The exact mechanism of Simvastatin in inducing bone formation is not fully understood. The differentiating effect on osteoblast is mediated by a BMP2 described by Mundy et al. [34]. Alternatively, *Wang et al.* [35] studies also have shown that Simvastatin induces phosphorylation of mitogen-activated-protein (MAP) kinase through the heat shock protein 27 (HSP-27). Our findings were similar to these earlier reports regarding the osteogenic effects of Simvastatin.

The previous histological findings for the control groups (machined and acid-etched) were similar to the present study [36]. Smooth surfaces promoted fibroblast and epithelial cell adhesion, whereas rough surfaces increased osteoblastic proliferation [37]. In the present work, fibrous tissue was also observed on the machined implants where direct bone

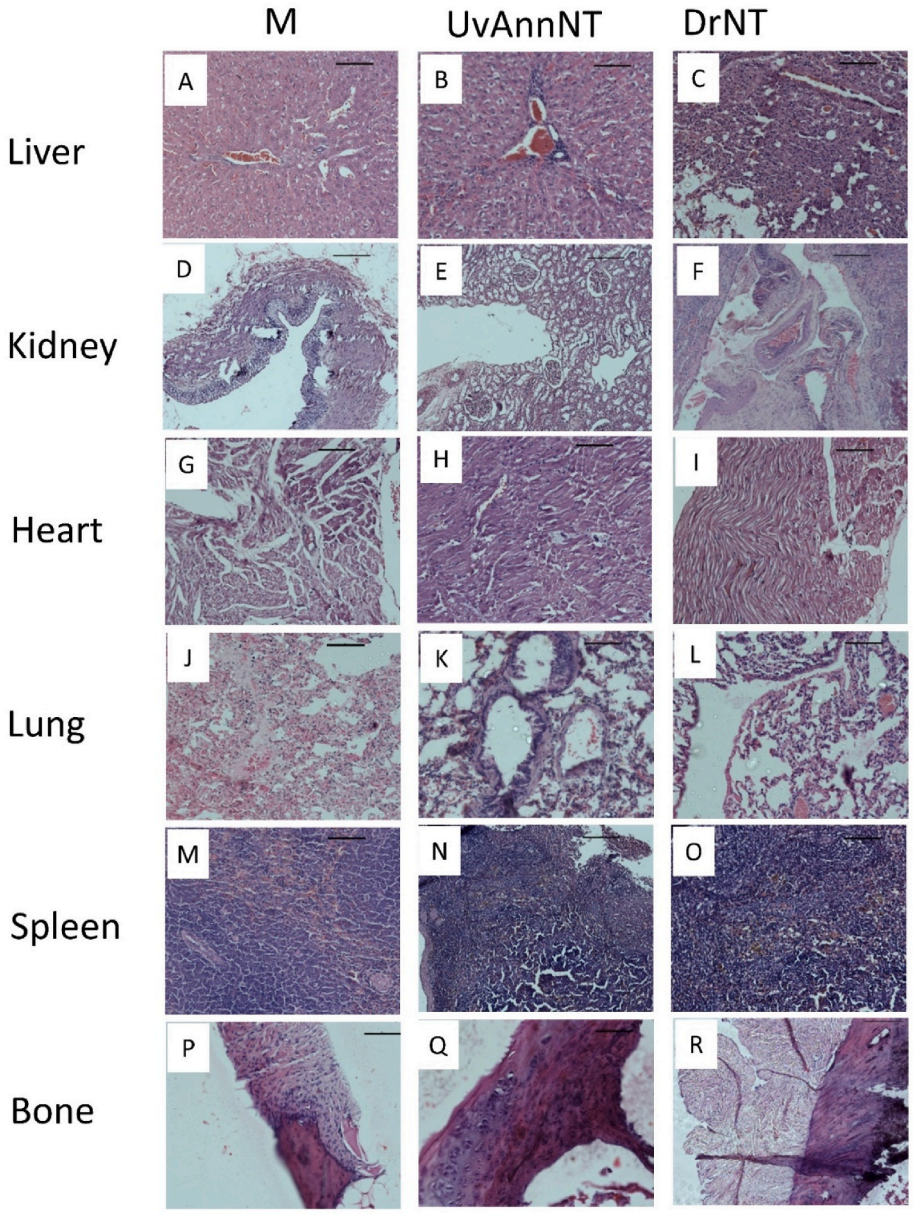

Fig. 15. HE staining of the Liver, Kidney, Heart, Lung, Spleen, and Bone of rabbits.

tissue apposition was present on the other group surfaces after 4 weeks of healing. Meanwhile, the findings of the nanotubes experimental group were also similar to previous studies. However, the effect of Simvastatin on osseointegration released through nanotubes was not studied in the past. The observed thick trabecular structure around the Simvastatin-loaded dental implants resulted in improved implant fixation. This thicker trabecular structure might have resulted from the reduction in the osteoclast and stimulation of osteoblastic activities as a consequence of the increased residual woven bone. As a result, bone density seems to be increased in the drug-loaded experimental group.

In the present study, both BIC% and BV% increased significantly between all the experimental groups. BV% may be increased because of the increased amount of bone in the experimental groups' medullary canal. The increased BIC% and BV% also contribute to increased implant stability and effectively disperse the occlusal force or other stresses.

In the present study, quantitative micro-CT and histomorphometry analysis were also correlated with the reverse torque observations. Reverse torque removal value is one of the indicators of both primary and secondary stability of implants in bone. However, the strength of the mechanical anchorage of screwed implants in bone varies with the implantation site, the healing rate, the roughness of the implant, and the bioactivity of the implant surface [38]. In the present research work, the reverse torque removal was measured on screw-shaped implants similar to those used in the clinical situation to avoid possible bias with different implant designs. As surface roughness also plays an important role in bone-implant integration and reverse torque removal values [39], nanotube implants used in the present study were anodized in such a way that the initial roughness of the surface was comparable to the acid-etched surface.

Previously it has been already reported that nanostructured surfaces with different nanotube diameters enhance the early bone tissue apposition as well as higher bone-implant anchorage in comparison to smooth titanium [40–43]. However, no study to date has compared the osseointegration of the titanium nanotubes dental implant surface loaded of optimized Simvastatin drug with classic SLA implant surface to the best of our knowledge. Overall, the results indicated that the nanotube and drug-loaded nanotube surfaces were better integrated into the bone than the standard SLA and machined control surface after 4 weeks of healing.

5. Conclusion

The present study evaluated the osseointegration of nanotube and Simvastatin drug-loaded nanotube dental implant surfaces, both in-vitro and in-vivo. The cytocompatibility studies, histomorphometric analysis, micro-CT, and reverse torque removal methods evaluated the osseointegration of different surface implants, and the results from all methods correlated well. This report showed that Simvastatin successfully accelerated the osteogenesis around titanium dental implants resulting in faster and stronger osseointegration at 4 weeks of healing only. The major limitation of this research work is that the study was conducted for short-term healing. But within the limitations, this study proved that Simvastatin eluting nanotubular dental implants g osseointegrated at a faster rate and thus paves the path for future long-term osseointegration studies, detailed toxicology and safety studies for drug-eluting nanotubular dental implants before clinical translation.

Animal ethical statement

This investigation followed all the institutional ethical guidelines (Guide for the Care and Use of Laboratory Animals) for the protection of animals and ethical approval for animal experimentation were taken from an ethical committee, All India Institute of Medical Sciences, New Delhi *(Ethical Clearance no. 25/IACE-1/2017)*.

CRediT authorship contribution statement

Pankaj Chauhan: Conceptualization, Methodology, Investigation, Writing – original draft, Writing – review & editing. **Alok Srivastava:** Methodology, Investigation, Visualization. **Pooja Bhati:** Methodology, Investigation. **Manish Chaturvedi:** Investigation, Resources. **Vinay Patil:** Investigation, Resources. **Sriram Kunnoth:** Investigation, Resources. **Nisha Kumari:** Investigation, Resources. **Vedpal Arya:** Investigation, Resources. **Madhur Pandya:** Investigation, Resources. **Mohit Agarwal:** Investigation, Resources. **Smiti Bhardwaj:** Investigation, Resources. **Farrukh Faraz:** Supervision, Resources. **Sanjay Chauhan:** Conceptualization, Writing – review & editing, Resources. **Mahesh Verma:** Conceptualization, Supervision, Funding acquisition. **Veena Koul:** Conceptualization, Writing – review & editing, Supervision. **Naresh Bhatnagar:** Conceptualization, Writing – review & editing, Supervision, Funding acquisition.

Declaration of competing interest

The authors confirm that there are no known conflicts of interest associated with this publication and there has been no significant financial support for this work that could have influenced its outcome. The author also confirm that this manuscript has not been published previously, and it is not under consideration for the publication elsewhere. All authors have confirmed the submission of this manuscript.

Acknowledgment and source of funding

The authors appreciate a generous grant aid by CSIR-NMITLI (New Millennium Industrial Technology Leadership Initiative), for developing an indigenous dental implant system in India.

References

[1] M. Kulkarni, A. Mazare, P. Schmuki, A. Iglič, Biomaterial surface modification of titanium and titanium alloys for medical applications, Nanomedicine 111 (2014) 111–136.
[2] C. Zhang, et al., Dental implants loaded with bioactive agents promote osseointegration in osteoporosis: a review, Front. Bioeng. Biotechnol. 0 (2021) 8.
[3] C.M. Díaz-Castro, et al., A non-interventional study documenting use and success of tissue level implants, Int. J. Environ. Res. Publ. Health 17 (2020) 1–13.
[4] C.N. Elias, Y. Oshida, J.H.C. Lima, C.A. Muller, Relationship between surface properties (roughness, wettability and morphology) of titanium and dental implant removal torque, J. Mech. Behav. Biomed. Mater. 1 (2008) 234–242.
[5] A. El-Banna, et al., Surface modification techniques of dental implants, in: *Dental Implants* 49–68, Elsevier, 2020, https://doi.org/10.1016/b978-0-12-819586-4.00004-4.
[6] Sohail Zafar, M. et al. Coatings Customized Therapeutic Surface Coatings for Dental Implants. doi:10.3390/coatings10060568.
[7] K. Subramanian, D. Tran, K.T. Nguyen, Cellular responses to nanoscale surface modifications of titanium implants for dentistry and bone tissue engineering applications, in: Emerging Nanotechnologies in Dentistry, second ed., Elsevier Inc., 2018 https://doi.org/10.1016/B978-0-12-812291-4.00008-X, 137–163.
[8] S. Ferraris, et al., Cytocompatible and anti-bacterial adhesion nanotextured titanium oxide layer on titanium surfaces for dental and orthopedic implants, Front. Bioeng. Biotechnol. 7 (2019) 1–12.
[9] K. Gulati, H.J. Moon, T. Li, P.T. Sudheesh Kumar, S. Ivanovski, Titania nanopores with dual micro-/nano-topography for selective cellular bioactivity, Mater. Sci. Eng. C 91 (2018) 624–630.
[10] B. Wu, Y. Tang, K. Wang, X. Zhou, L. Xiang, Nanostructured titanium implant surface facilitating osseointegration from protein adsorption to osteogenesis: the example of TiO2 NTAs, Int. J. Nanomed. 17 (2022) 1865–1879.
[11] D. Losic, et al., Titania nanotube arrays for local drug delivery : recent advances and perspectives, Expet Opin. Drug Deliv. 12 (2015) 103–127.
[12] L. Xia, et al., In vitro and in vivo studies of surface-structured implants for bone formation, Int. J. Nanomed. 7 (2012) 4873–4881.
[13] N. Blanc-Sylvestre, P. Bouchard, C. Chaussain, C. Bardet, Pre-clinical models in implant dentistry: past, present, future, Biomedicines 9 (2021).
[14] M. Rahmati, et al., Coating doxycycline on titanium-based implants: two in vivo studies, Bioact. Mater. 5 (2020) 787–797.
[15] R. Chiesa, et al., In vitro and in vivo performance of a novel surface treatment to enhance osseointegration of endosseous implants, Oral Surg. Oral Med. Oral Pathol. Oral Radiol. Endod. 103 (2007) 745–756.
[16] A. Parsa, N. Ibrahim, B. Hassan, P. van der Stelt, D. Wismeijer, Bone quality evaluation at dental implant site using multislice CT, micro-CT, and cone beam CT, Clin. Oral Implants Res. 26 (2015) e1–e7.
[17] T. He, et al., A comparison of micro-CT and histomorphometry for evaluation of osseointegration of PEO-coated titanium implants in a rat model, Sci. Rep. 7 (2017) 1–11.
[18] Q. Wang, et al., Multi-scale surface treatments of titanium implants for rapid osseointegration: a review, Nanomaterials 10 (2020) 1–27.
[19] F. Wang, C. Li, S. Zhang, H. Liu, Role of TiO_2 nanotubes on the surface of implants in osseointegration in animal models: a systematic review and meta-analysis, J. Prosthodont. 29 (2020) 501–510.
[20] Anil, S. et al. Drug Delivery Systems in Bone Regeneration and Implant Dentistry.
[21] S. Dundar, A. Bozoglan, Evaluation of the effects of topically applied simvastatin on titanium implant osseointegration, J Oral Biol Craniofac Res 10 (2020) 149–152.
[22] J.H. Jun, et al., Improvement of osseointegration by ultraviolet and/or simvastatin treatment on titanium implants with or without bone graft materials, Materials 14 (2021) 3707, 14, 3707 (2021).
[23] G. Li, et al., Strontium and simvastatin dual loaded hydroxyapatite microsphere reinforced poly(ε-caprolactone) scaffolds promote vascularized bone regeneration, J. Mater. Chem. B 11 (2023) 1115–1130.
[24] S.A. Gehrke, G.W. Marin, Biomechanical evaluation of dental implants with three different designs: removal torque and resonance frequency analysis in rabbits, Ann. Anat. 199 (2015) 30–35.
[25] J.W. Koh, J.H. Yang, J.S. Han, J.B. Lee, S.H. Kim, Biomechanical evaluation of dental implants with different surfaces: removal torque and resonance frequency analysis in rabbits, Journal of Advanced Prosthodontics 1 (2009) 107–112.
[26] J.L. Calvo-Guirado, et al., Biomechanical and histological evaluation of four different titanium implant surface modifications: an experimental study in the rabbit tibia, Clin. Oral Invest. 18 (2014) 1495–1505.
[27] M. Verma, et al., Dental Implant System, 2008.
[28] P. Chauhan, V. Koul, N. Bhatnagar, Design and development of indigenous dental implant system: from research to reality, Trends Biomater. Artif. Organs 32 (2018) 51–62.
[29] P. Chauhan, V. Koul, N. Bhatnagar, Effect of acid etching temperature on surface physiochemical properties and cytocompatibility of Ti6Al4V ELI alloy, Mater. Res. Express 6 (2019), 105412.
[30] P. Chauhan, V. Koul, N. Bhatnagar, Critical role of etching parameters in the evolution of nano micro SLA surface on the Ti6Al4V alloy dental implants, Materials 14 (2021) 6344, 14, 6344 (2021).
[31] D. Regonini, A. Jaroenworaluck, R. Stevens, C.R. Bowen, Effect of heat treatment on the properties and structure of TiO2 nanotubes: phase composition and chemical composition, Surf. Interface Anal. 42 (2010) 139–144.
[32] V.F. Mauro, J. L. Simvastatin MacDonald, A review of its pharmacology and clinical use, Ann. Pharmacother. 25 (1991) 257–264.
[33] A. Wennerberg, T. Albrektsson, C. Johansson, B. Andersson, Experimental study of turned and grit-blasted screw-shaped implants with special emphasis on effects of blasting material and surface topography, Biomaterials 17 (1996) 15–22.
[34] G. Mundy, et al., Stimulation of bone formation in vitro and in rodents by statins, Science 286 (1979) 1946–1949, 1999.
[35] X. Li, Q. Cui, C. Kao, G.J. Wang, G. Balian, Lovastatin inhibits adipogenic and stimulates osteogenic differentiation by suppressing PPARγ2 and increasing Cbfa1/Runx2 expression in bone marrow mesenchymal cell cultures, Bone 33 (2003) 652–659.

[36] F. Takeshita, Y. Ayukawa, S. Iyama, K. Murai, T. Suetsugu, Long-term evaluation of bone-titanium interface in rat tibiae using light microscopy, transmission electron microscopy, and image processing, J. Biomed. Mater. Res. 37 (1997) 235–242.
[37] B.D. Boyan, et al., in: The Titanium-Bone Cell Interface in Vitro: the Role of the Surface in Promoting Osteointegration, Springer, Berlin, Heidelberg, 2001, https://doi.org/10.1007/978-3-642-56486-4_17, 561–585.
[38] Q. Wang, et al., Multi-scale surface treatments of titanium implants for rapid osseointegration: a review, Nanomaterials 10 (2020) 1–27.
[39] S.F. Lamolle, M. Monjo, S.P. Lyngstadaas, J.E. Ellingsen, H.J. Haugen, Titanium implant surface modification by cathodic reduction in hydrofluoric acid: surface characterization and in vivo performance, J. Biomed. Mater. Res. 88 (2009) 581–588.
[40] S. Lavenus, et al., Cell differentiation and osseointegration influenced by nanoscale anodized titanium surfaces, Nanomedicine 7 (2012) 967–980.
[41] L.M. Bjursten, et al., Titanium dioxide nanotubes enhance bone bonding in vivo, J. Biomed. Mater. Res. 92 (2010) 1218–1224.
[42] E.P. Su, D.F. Justin, C.R. Pratt, Effects of titanium nanotubes on the osseointegration, cell differentiation, mineralisation and antibacterial properties of orthopaedic implant surfaces, Bone and Joint Journal 100B (2018) 9–16.
[43] K.D. Yun, et al., Titanium dioxide nanotube modified implants: an animal study on bone formation, J. Nanosci. Nanotechnol. 13 (2013) 3864–3867.